GEOPHYSICS, VOL. 89, NO. 1 (JANUARY-FEBRUARY 2024); P. F23–F39, 22 FIGS., 2 TABLES.
10.1190/GEO2023-0105.1

PyMERRY: A Python solution for an improved interpretation of electrical resistivity tomography images

Maxime Gautier[1], Stéphanie Gautier[1], and Rodolphe Cattin[1]

ABSTRACT

Electrical resistivity tomography (ERT) is a widely used geophysical method for studying geologic hazards, civil engineering, and environmental remediation. It provides information about the subsurface's resistivity distribution by analyzing electrical data collected at the surface or in boreholes. However, interpreting ERT images can be complex due to ambiguities in their resolution. To address this issue, we develop a postprocessing method called Python iMprovement of Electrical Resistivity tomography ReliabilitY (PyMERRY) to improve the reliability of ERT images. The PyMERRY code can be applied to any 2D resistivity model obtained from ERT inversion software. It computes a coverage mask that defines the domain well constrained by the data and the inversion process. It also evaluates the resistivity uncertainties in the ERT models. In addition to the sensitivity approaches, PyMERRY provides low- and high-resistivity values for all covered cells. Synthetic tests indicate that the approach is efficient and highlight the importance of resistivity contrasts, mesh selection, electrode spacing, and profile length in the reliability of ERT images. Compared with previous studies, using PyMERRY in south-central Bhutan allows a more accurate interpretation of ERT images. It confirms a high-resistivity contrast across the topographic frontal thrust and reveals the existence of small-scale variations.

INTRODUCTION

Soil and substrate characterization is essential to improve the assessment of anthropogenic and natural hazards. For several decades, multidisciplinary strategies integrating geologic observation, mechanical investigation, and geophysical methods have been the most effective approaches to constraining subsurface layers (e.g., Demanet et al., 2001; McLachlan et al., 2017; Romero-Ruiz et al., 2018; Pazzi et al., 2019; Whiteley et al., 2019). Among these geophysical methods, electrical resistivity tomography (ERT) is a standard approach to assess lithology, fluid contents, or chemistry in the shallow subsurface (tens of meters). In particular, ERT is widely used to characterize the geometry of geologic structures such as faults (e.g., Nguyen et al., 2005; Suski et al., 2010; Villani et al., 2015; Drukpa et al., 2018) or landslide bodies (e.g., Friedel et al., 2006; Jomard et al., 2010; Perrone et al., 2014), and to explore the ground in geotechnical engineering (e.g., Daily and Ramirez, 2000; Fortier and Bolduc, 2008; Danielsen and Dahlin, 2010). Because time-lapse ERT provides further information on time changes of the resistivity pattern in the subsurface, this geophysical technique is also a relevant tool to investigate dynamic processes such as water flows (e.g., Binley et al., 2001; Nguyen et al., 2009; Wilkinson et al., 2010; Singha et al., 2015; Watlet et al., 2018; Palacios et al., 2020; Lapenna and Perrone, 2022), gas storage (e.g., Bergmann et al., 2012; Denchik et al., 2014; Zhou et al., 2020), and environmental remediation (e.g., Kuras et al., 2016; Dimech et al., 2022; Lévy et al., 2022).

In a general sense, the ERT technique consists of recording apparent resistivities and inverting them to map the resistivity distribution at depth and capture possible time changes. Many software packages, such as Res2DInv (Loke and Barker, 1996), R2 (Binley and Slater, 2020), or PyGIMLi (Rücker et al., 2017) are now available to carry out the data inversion following a gradient-based approach (LaBrecque et al., 1999). ERT models are then interpreted to define the complex interactions between various geologic and hydrogeologic processes.

Despite the success of the ERT method, the quality assessment of resistivity models remains an open and challenging question. The

Peer-reviewed code related to this article can be found at this paper's Supplemental Materials link.
Manuscript received by the Editor 21 February 2023; revised manuscript received 15 September 2023; published ahead of production 24 October 2023; published online 13 December 2023.
[1]University of Montpellier, Géosciences Montpellier — CNRS, Montpellier, France. E-mail: maxime.gautier@umontpellier.fr (corresponding author); stephanie.gautier-raux@umontpellier.fr; rodolphe.cattin@umontpellier.fr.

robustness of the ERT results depends on various factors such as the source and receiver geometry, measurement errors due to the acquisition system, electrode mislocations, field conditions (including soil moisture, topography, and temperature), or the resistivity pattern in the subsurface (e.g., Furman et al., 2003; Zhou and Dahlin, 2003; Oldenborger et al., 2005; LaBrecque et al., 2007; Tso et al., 2017). Although using deterministic and linearized inversion schemes guarantees a fast convergence toward a solution, such inversion approaches do not allow accurate uncertainty assessments (Ramirez et al., 2004). The lack of reliable information on the accuracy and spatial resolution of ERT models can lead to misinterpretations. Standard ERT inversion software proposes a sensitivity analysis that reflects how resistivity variations at depth could influence the measured apparent resistivity values. This indicator gives us helpful insight into the quality of the recovered model. However, this sensitivity analysis does not give estimates of model uncertainty or spatial resolution.

We propose a new approach for assessing solution quality in resistivity tomography to overcome this limitation and to allow for a more accurate interpretation of ERT models. In this study, the open-source library PyGIMLi is used to develop a new tool that relies on (1) the computation of a coverage mask to delineate investigated zones and quantify the spatial sampling density and (2) the calculation of the uncertainties of the resistivity model in the covered zones. First, we describe the complete procedure for this new postprocessing code. Then, we illustrate the relevance of this new tool from synthetic tests associated with a well-constrained resistivity model. Finally, we revisit the ERT models obtained in south-central Bhutan by Drukpa et al. (2018) and discuss their reliability in inferring the geometry of the topographic frontal thrust (TFT), an active fault that experienced at least two major earthquakes in the last millennium (Le Roux-Mallouf et al., 2016).

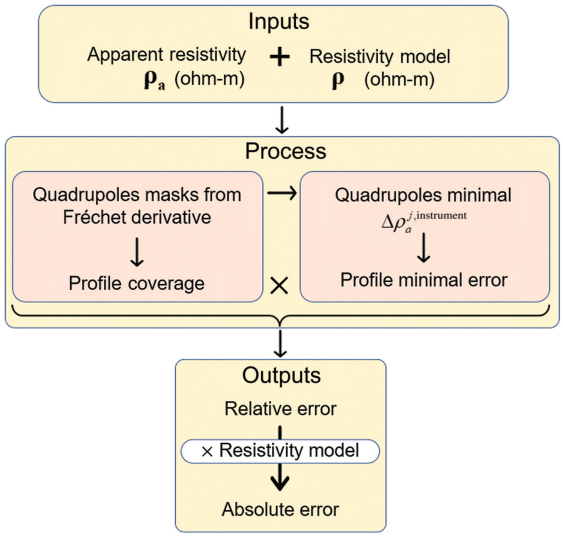

Figure 1. Workflow describing the three main steps of the PyMERRY code, including input data, model information, processing, and output resistivity error values. The apparent resistivity data and the resistivity model are denoted as $\boldsymbol{\rho}_a$ and $\boldsymbol{\rho}$, respectively. The apparent resistivity variation detectable by the instrument used in the field is denoted as $\Delta\rho_a^{j,\text{instrument}}$.

METHODS

Quantifying the ambiguity inherent in ERT sections is a significant challenge. Here, we propose a new code to better characterize the reliability of these images based on spatial coverage and instrumental accuracy. This tool is called Python iMprovement of Electrical Resistivity tomography ReliabilitY (PyMERRY). After briefly reviewing some theoretical definitions and concepts, we describe its flowchart (Figure 1).

Theoretical considerations

In the field, data acquisition is conducted with different electrode configurations (e.g., Wenner-Schlumberger, dipole-dipole, and gradient configurations), called electrode arrays, along the same profile (e.g., Furman et al., 2003; Zhou and Dahlin, 2003). A survey can be carried out using an automatic multielectrode system, which allows for repeated measurements of apparent resistivity for all combinations of four electrodes called quadrupoles for the chosen configuration.

At the midpoint of one quadrupole, the depth of investigation (DOI) is the depth contributing the most to the apparent resistivity recorded at the surface according to Roy and Apparao (1971). Oldenburg and Li (1999) compute a DOI to delineate the area where the data well constrain the resistivity model.

Sensitivity is a common criterion for assessing the quality of ERT models. For a quadrupole, the sensitivity characterizes the effect of resistivity changes at depth on the potential field and the apparent resistivity measured at the surface (Park and Van, 1991; Loke and Barker, 1995). The mathematical tool used to evaluate the quadrupole sensitivity is based on the Fréchet derivatives linking resistivity model variations and forward-modeled data changes. McGillivray and Oldenburg (1990) propose an analytical expression of the Fréchet derivative for a 1D resistivity model. The evaluation of the sensitivity in a heterogeneous medium requires numerical approaches, such as the direct current forward matrix technique proposed by Ghanati and Fallahsafari (2022).

At the profile scale, quadrupole sensitivities are summed up to estimate the sensitivity map (e.g., Gance et al., 2016; Ronczka et al., 2017). This map is then used to delineate the resolved area and assess the reliability of ERT models. In particular, the sensitivity map provides valuable information on the lack of spatial resolution at depth, where the sensitivity is poor (Binley and Kemna, 2005). However, converting the sensitivity map into a resistivity error map is more complex. In the following, we propose an alternative approach to these sensitivity analyses for assessing resistivity model uncertainties.

Input parameters

Two pieces of input information are necessary for the PyMERRY code (Figure 1). First, it needs the data recorded in the field that refer to the n measurements of apparent resistivity $\boldsymbol{\rho}_a$ and the related electrode quadrupole information, including the electrode location and configuration (note that only models with no topographic variation and Wenner, Wenner-Schlumberger, dipole-dipole, and gradient configurations are supported in the current version v1.0 of PyMERRY). This data set must be the same as that used in the inversion process. The second input is the resistivity model $\boldsymbol{\rho}$ computed by inversion software, such as R2, Res2DInv, or PyGIMLi,

which includes the inversion-derived resistivity distribution and the 2D mesh used for the inversion.

Coverage computation

The first step of the PyMERRY process consists of computing a parameter called the coverage (Figure 1). This value describes how apparent resistivity measurements, recorded by the different quadrupoles of an ERT survey, sample the subsurface. The coverage delineates the well-resolved regions and limits computation only to the investigated space.

We consider the electrode information, the resistivity distribution $\boldsymbol{\rho}$, and the 2D mesh of the inverted ERT model. A complete table of used symbols is shown in Appendix A. We solve a forward problem of the electrical propagation equation in the subsurface (Telford et al., 1990) using a finite-element method to obtain the electrical potential field $\mathbf{U}$ (e.g., Rücker et al., 2017). From the potential field, we compute two physical quantities: a theoretical resistivity value $\boldsymbol{\rho}_{\mathbf{a}}^{\mathbf{th}}$ related to the electrode configuration and the current density field $\mathbf{J}$ as

$$\mathbf{J} = -\frac{1}{\boldsymbol{\rho}}\nabla\mathbf{U}. \tag{1}$$

According to Park and Van (1991), the link between a resistivity variation $\delta\boldsymbol{\rho}$ in the model and a potential variation $\delta\mathbf{U}$ in an elementary volume dV considering one injection electrode (A) and one measurement electrode (M) is given by

$$\frac{\delta\mathbf{U}}{\delta\boldsymbol{\rho}} = \int_V \mathbf{J}_\mathrm{A}\cdot\mathbf{J}_\mathrm{M}dV, \tag{2}$$

where the inner product $\mathbf{J}_\mathrm{A}\cdot\mathbf{J}_\mathrm{M}$ inside the integral symbol is one expression of the Fréchet derivative. For quadrupole j, by combining A-B injection electrodes and M-N measurement electrodes, the Fréchet derivative $\mathbf{F}^j$ is

$$\mathbf{F}^j = \mathbf{J}_\mathrm{A}^j\cdot\mathbf{J}_\mathrm{M}^j - \mathbf{J}_\mathrm{B}^j\cdot\mathbf{J}_\mathrm{M}^j - \mathbf{J}_\mathrm{A}^j\cdot\mathbf{J}_\mathrm{N}^j + \mathbf{J}_\mathrm{B}^j\cdot\mathbf{J}_\mathrm{N}^j. \tag{3}$$

We define F_i^j as the Fréchet derivative associated with cell i and quadrupole j. If $|F_i^j|$ is close to zero, it indicates that measurements recorded using quadrupole j are highly insensitive to resistivity changes in cell i.

The absolute value of the Fréchet derivative $|F_\mathrm{DOI}^j|$ at the DOI depends on the distance L between the first and the last electrode for the quadrupole j, as defined by Barker (1989) (Table 1). In our approach, $|F_\mathrm{DOI}^j|$ is a threshold. Only cells with $|F_i^j| > |F_\mathrm{DOI}^j|$ are considered covered. Figure 2 shows the approach by showing the DOI location, the associated threshold $|F_\mathrm{DOI}^j|$, and the related covered region computed for one quadrupole in the Wenner configuration on a triangular mesh.

In contrast to conventional software, we do not analyze the sensitivity based on the Fréchet derivative values directly. We instead use these values associated with quadrupole j to deduce a binary mask $\mathbf{m}^j$. This mask contains the m_i^j values for cells i. We set $m_i^j = 1$ and $m_i^j = 0$ for covered and uncovered cells, respectively. Finally, the normalized coverage map is derived by summing the contributions of all the quadrupoles:

$$C_i = \frac{\sum_{j=1}^n m_i^j}{\max\left(\sum_{j=1}^n m_i^j\right)}, \tag{4}$$

where n is the number of quadrupoles. The coverage C_i ranges between zero and one for uncovered and fully sampled cells, respectively. The PyMERRY coverage allows us to delineate the covered domain as the area where $C_i > 0$.

We use the geometry and the coverage values in the next steps of the PyMERRY process. In particular, the coverage saves computational time when evaluating errors by limiting calculation only to the covered cells.

Array error assessment

The second step of the PyMERRY code concerns a reliable assessment of errors in the resistivity model to quantify the uncertainty of the ERT image (Figure 1). For each cell i, the strategy consists of estimating the minimum resistivity changes detectable by a measuring device located at the ground surface. These minima are associated with errors in the resistivity model due to resistivity heterogeneity at depth and electrode configuration.

Similar to any device, resistivity meters have instrumental specifications that limit their ability to detect slight variations in apparent resistivity measurements. To integrate the accuracy of the measuring device, we introduce a value $\boldsymbol{\rho}_{\mathbf{a}}^{\mathbf{var}}$, the apparent resistivity

Table 1. The DOI in a homogeneous half-space determined by Barker (1989) for different electrode configurations.

Configuration	DOI (m)
Wenner	0.17 L
Dipole-dipole	0.25 L
Schlumberger	0.19 L

The distance between the first and the last electrode of a quadrupole is the L parameter.

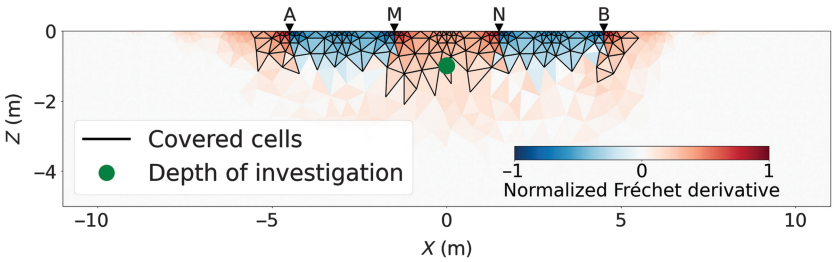

Figure 2. Example of a Wenner quadrupole mask computed by the PyMERRY code. The color scale shows the Fréchet derivative values normalized between the minimal and maximal values. The green dot indicates the location of the DOI at the midpoint of the quadrupole. The black lines delineate the covered cells. Small black triangles give the locations of A-B and M-N, the injection and potential electrodes, respectively. Note that although normalization is performed for display purposes, it is not necessary in this study, as the Fréchet derivatives calculated are compared to the DOI threshold value to create a mask.

measurement considering a resistivity variation in one cell of the model. A resistivity change at depth is then detectable for

$$\Delta\rho_a^{j,\text{instrument}} = |\rho_a^{j,\text{th}} - \rho_a^{j,\text{var}}| > t^j, \quad (5)$$

where t^j is the instrumental threshold for each quadrupole j. We used the Ohm's law to define this threshold from the nominal resistivity meter relative accuracies in percentage α and β for the transmitted current intensity I and received potential U, respectively. Most of the technical instrumental manuals provide these nominal accuracies. These values are minimal, as they do not consider field conditions and measurement errors. Users could adjust these values for a specific ERT survey by conducting field tests to ensure accuracy. Appendix B provides a detailed explanation of the threshold calculation steps.

Considering the instrumental detectability threshold t^j, we assess for each quadrupole j and covered cell i the minimum detectable resistivity variation. First, we test the effects of positive $\delta\rho_i^{j,+}$ and negative $\delta\rho_i^{j,-}$ variation ranging from 0 to ρ_i on the apparent resistivity measurement $\rho_a^{j,\text{var}}$. Next, we define the detectable resistivity variation $|\delta\rho_i^j/\rho_i|$ as the minimum value between $|\delta\rho_i^{j,+}/\rho_i|$ and $|\delta\rho_i^{j,-}/\rho_i|$ reaching the instrumental detectability threshold. Finally, we determine $|\delta\rho_i/\rho_i|$, the minimum $|\delta\rho_i^j/\rho_i|$ required to exceed the instrument's detection threshold in each cell whatever the considered quadrupole.

For example, we apply this approach to a Wenner array (Figure 3). This test points out a different trend for positive and negative resistivity perturbations. Compared with negative perturbations, a resistivity increase favors a more linear relationship between $|\Delta\rho_a^{j,\text{instrument}}|$ and $|\delta\rho_i^j/\rho_i|$. Our result shows an asymptotic behavior of $|\Delta\rho_a^{j,\text{instrument}}|$ for a fully conductive cell, i.e., when $\delta\rho_i^{j,-}$ tends to $-\rho_i$.

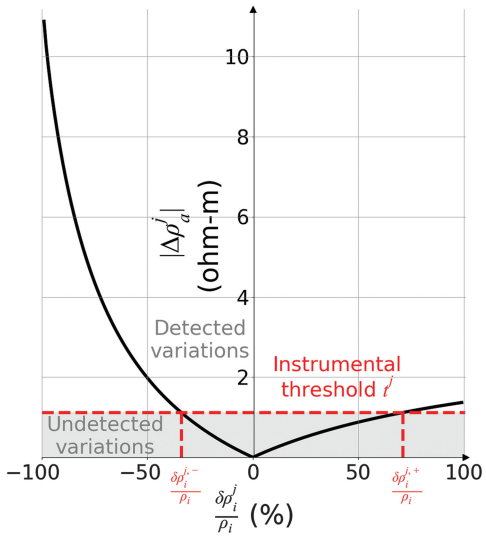

Figure 3. Example of the relationship between the resistivity variation in cell i and the apparent resistivity measured by the quadrupole j. The black line represents the apparent resistivity variation $|\Delta\rho_a^j|$ due to negative and positive resistivity variation $\delta\rho_i^j/\rho_i$. The horizontal dashed red line represents the instrumental detection threshold t^j. The labels $\delta\rho_i^{j,+}/\rho_i$ and $\delta\rho_i^{j,-}/\rho_i$ indicate the minimal detectable resistivity variations. The gray-shaded rectangle delineates the area of undetected variation.

Output resistivity error values

The relative error map is obtained from

$$\boldsymbol{\varepsilon}_{\text{relative}} = \left|\frac{\boldsymbol{\delta\rho}}{\boldsymbol{\rho}}\right|, \quad (6)$$

and the absolute error is obtained from

$$\boldsymbol{\varepsilon}_{\text{absolute}} = \boldsymbol{\rho}\boldsymbol{\varepsilon}_{\text{relative}}. \quad (7)$$

These two types of errors are complementary. Indeed, the relative error is the most suitable to interpret images with high-resistivity contrast. The absolute error is more valuable to characterize the properties of the medium in terms of lithology, fracturing, or water content.

RESULTS

Resistivity model, synthetic data generation, and inversion parameters

To test our approach, PyMERRY is applied to the 2D tabular model provided in the "2D ERT modeling and inversion" section of the PyGIMLi documentation website (Rücker et al., 2022), which is called the "true" model in the following.

We consider a vertical cross section 100 m long and 50 m deep (Figure 4a). Three horizontal layers compose this model: (1) a surface layer (top layer [TL]) 1 m thick with a resistivity of 100 ohm-m, (2) an intermediate layer (middle layer [ML]) 4 m thick with a resistivity of 75 ohm-m, and (3) a deep layer (bottom layer [BL]) with a resistivity of 50 ohm-m. ML also includes two anomalous bodies: a high-resistivity body (HB) and a low-resistivity body (LB) with resistivities of 150 and 25 ohm-m, respectively. HB is a horizontally elongated ellipse 8 m long with a maximum thickness of 2 m. LB is a body with a more complex geometry, 8 m long, and a varying thickness that can locally reach 3 m.

This cross section is discretized with a 3544 triangular cells mesh, refined near the electrodes, as the PyGIMLi documentation website advises. Based on this meshed cross section, we generate a data set of 171 apparent resistivities, assuming a profile of 21 electrodes at the same elevation with a 1.5 m spacing in a dipole-dipole configuration. Normally distributed random noise is added to the synthetic data set with a mean of zero and a standard deviation of $0.01 \times \boldsymbol{\rho}_\mathbf{a}$. The low noise level enables the reconstruction of an ERT inverted model close to the true model; the errors computed by the PyMERRY software only reflect the ERT images' uncertainties linked to the inversion-derived resistivity pattern and the chosen dipole-dipole electrode configuration.

We perform an inversion of this synthetic data set using a classic Gauss-Newton algorithm with regularization (Rücker et al., 2017). The dimensionless regularization factor λ controls the smoothing in the final image ($\lambda = 0$, no smoothing). We choose the default value for the regularization parameter $\lambda = 20$. The inversion is carried out on a second mesh to avoid considering any a priori information as in a real case. This second mesh contains finer cells to achieve better image resolution. Moreover, it encompasses half of the profile laterally and at depth to avoid edge effects. We use the default implementation of the starting model. We consider a homogeneous medium 60 m long and 15 m thick composed of 6624 triangular cells, with a resistivity of approximately

68 ohm-m, a value equal to the median of apparent resistivity data. After three iterations, the obtained resistivity model properly fits the data with a root mean square of approximately 0.44% and the chi-squared value decreasing from approximately 504 to 0.19 (for the definition of the chi-square used in PyGIMLi, see Appendix C).

Comparison of the resulting and the true model

We discuss the reliability of the ERT images by comparing the obtained and true model (Figure 4a and 4b). The inverted resistivity model images some of the true model's features relatively well. Indeed, the inverted model suggests a surface layer of approximately 1 m with a resistivity of 90 ohm-m beneath the electrodes, which can be related to TL. The two anomalous bodies are also well located. However, we can note significant differences. Outside the electrode line, the inversion does not recover the layered structure of the true model. Underneath the electrodes, the BL-ML boundary and the LB shape are not correctly imaged. Finally, except for TL and ML, the obtained resistivities deviate from those of the true model with magnitudes of approximately 10, 60–80, and 90 ohm-m for LB, BL, and HB, respectively. A smearing effect associated with resistivity contrasts can partly explain these deviations.

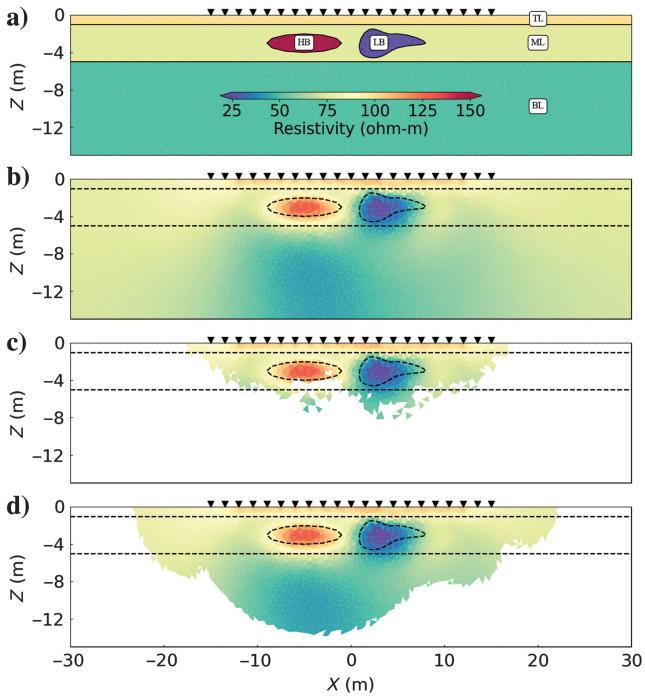

Figure 4. Synthetic test and associated masks. (a) True model composed of five bodies: TL with a resistivity of 100 ohm-m, ML with a resistivity of 75 ohm-m, BL with a resistivity of 50 ohm-m, high-resistivity body (HB) of 150 ohm-m, and low-resistivity body (LB) of 25 ohm-m. The black triangles show the electrode locations. The color scale is associated with medium resistivity. (b) The resistivity model obtained from the inversion of the synthetic data set using PyGIMLi. The dotted black lines represent the contour of the true model bodies. (c) The same as (b), with a mask based on sensitivity analysis. (d) The same as (b), with a mask defined by the PyMERRY coverage.

Reliability of inversion results

The true model is unknown when the inversion is associated with data acquired in the field. Alternative approaches are then needed to quantify the reliability of the ERT image. In the following, we apply our approach to the synthetic case presented previously to validate the reliability criteria implemented in PyMERRY. In this case study, one run with the PyMERRY code takes approximately 10 min on a 16-core central processing unit (CPU) personal computer.

Unmasked cells definition

As mentioned in the "Methods" section, part of the resulting ERT image must be masked to avoid misinterpretation (Figure 4c and 4d). In PyGIMLi and most ERT inversion codes, this mask is defined at the profile scale from the calculated sensitivity map and a threshold based on the DOI. The first solution is calculating the sensitivity map associated with a homogeneous half-space. In this case, the sensitivity decreases with depth, i.e., the distance to the electrodes (Figure 5a). The unmasked area shows a trapezoidal shape defined by the profile's length and the maximum investigation depth.

The model studied here does not verify the hypothesis of a homogeneous medium. Thus, the mask is based on the sensitivity map computed at the last inversion iteration (Günther et al., 2006). Because current lines are preferentially deflected into low-resistivity regions (Telford et al., 1990), this approach highlights the contribution of low-resistivity cells. The resistivity distribution mainly

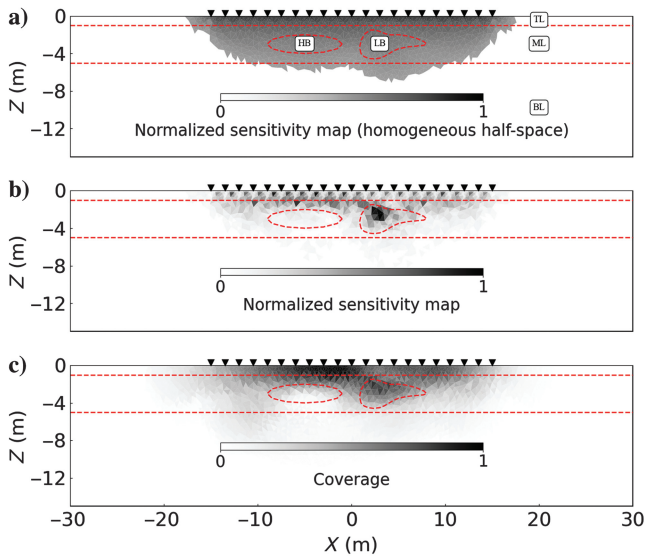

Figure 5. Synthetic test and resolution of unmasked cells based on sensitivity maps and coverage. We display the sensitivity maps and coverages with a linear normalization between minimal and maximal values. Body names TL, ML, BL, HB, and LB are shown in Figure 4. The black triangles show the electrode positions. The dotted red lines highlight the bodies' location and shape of the true model. The gray color scale is associated with the normalized value of either sensitivity or coverage. (a) The sensitivity map computed on a homogeneous medium assuming a resistivity of approximately 72 ohm-m, a value equal to the median of apparent resistivity data. (b) The sensitivity map computed on the nonhomogeneous model plotted in Figure 4. (c) Coverage calculated from the PyMERRY code.

controls the sensitivity map. The more resistive (conductive) an area is, the lower (higher) its sensitivity (Figure 5b). The mask is also defined with a sensitivity threshold associated with the DOI. Compared to the homogeneous medium, the unmasked zone's shape is more complex, with a strong asymmetry due to the presence of two anomalous bodies. The well-constrained zone is thicker near LB than HB. The sensitivity distribution in TL illustrates the main limitation of this approach. Indeed, the TL layer being more resistive than ML, its sensitivity must be lower. However, TL being closer to the electrodes, its sensitivity must be higher. As shown in Figure 2, the Fréchet derivatives associated with a quadrupole have the highest magnitude at the surface near the electrodes and change sign just below the electrodes. This results in high sensitivities between the electrodes and very low sensitivities just below despite the shallow depth of TL (Figure 5b). This explains why the obtained mask has poorly defined resistivities for cells in TL close to the electrodes.

The PyMERRY approach significantly improves the definition of the mask to be used. Similar to the conventional methods described previously, PyMERRY coverage considers the medium's heterogeneity and defines the mask from the sensitivity and the DOI. However, it differs from these approaches because the coverage is not based on the sensitivity map but is computed by summing individual masks associated with each quadrupole to obtain the coverage at the profile scale (see equations 3 and 4). Similar to the normalized sensitivity map, the PyMERRY coverage has an asymmetric shape associated with HB and LB (Figure 5b and 5c). It also avoids the main limitations of these methods: (1) by not masking the cells close to the electrodes, with coverage that decreases with depth, and (2) by keeping more cells in the deeper zone BL.

To test the relevance of the PyMERRY mask, we compare the resistivity distribution obtained for all cells and unmasked cells of the true model bodies (Figure 6). This mask has no impact on extreme resistivity values 25 and 150 ohm-m associated with HB and LB, respectively (Figure 6a–6d). The mask has no significant effect on values close to the mean resistivity in ML (Figure 6c). In contrast, the PyMERRY mask plays a significant role in the resistivity obtained in TL and BL. In these bodies, the resistivity distribution is bimodal. The PyMERRY coverage mask hides no relevant resistivity values in the model. For the two bodies, our approach keeps only the distribution peak closer to the true value (Figure 6b–6e).

Resistivity error assessment

The PyMERRY mask hides the uncovered cells. However, the well resolved and the true resistivities may not be consistent (Figures 4 and 5). For example, resistivities of 30–55 versus 25 ohm-m in the true model, 90–130 versus 150 ohm-m, are obtained in LB and HB, respectively. The absolute error $\boldsymbol{\varepsilon_{absolute}}$ computed with PyMERRY complements the resolution criterion. This parameter allows us to quantify the error by calculating for each cell the minimum and maximum likely value of resistivity (Figure 7).

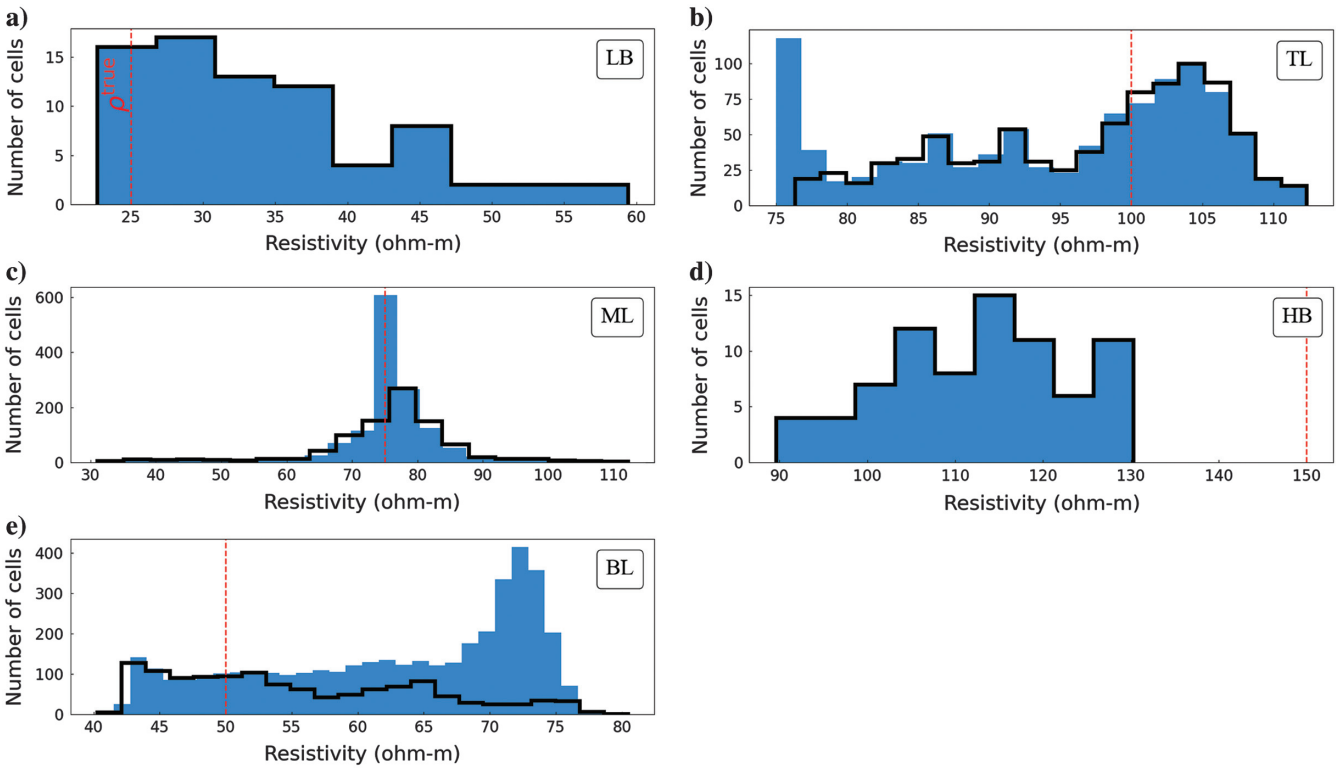

Figure 6. Effects of the PyMERRY mask on the resistivity distribution obtained in each body of the true model. The blue and black histograms are related to all cells and covered cells only (i.e., unmasked), respectively. Body names TL, ML, BL, HB, and LB are shown in Figure 4. The dotted red line shows the true resistivity ρ^{true}. (a) Resistivity distribution obtained in LB, (b) the same as (a) for TL, (c) the same as (a) for ML, (d) the same as (a) for HB, and (e) the same as (a) for BL.

The surface layer TL being close to the electrodes, we obtain a small deviation with distributions for $\boldsymbol{\rho} - \boldsymbol{\varepsilon}_{\mathbf{absolute}}$, $\boldsymbol{\rho}$, and $\boldsymbol{\rho} + \boldsymbol{\varepsilon}_{\mathbf{absolute}}$ centered on 90 and 120 ohm-m. In this layer, our result suggests a well-constrained resistivity in good agreement with the true model (Figure 7b). Conversely, the three distributions differ significantly for the other bodies, leading to a large error with an amplitude $\boldsymbol{\varepsilon}_{\mathbf{absolute}}$ close to $\boldsymbol{\rho}$.

We propose to improve this error assessment by relying on a classical bias of inversion methods: the smearing effect that produces a blurred image. The obtained resistivities, which are higher (lower) than the mean resistivity $\overline{\rho}$, are therefore often under (over) estimated. We use three types of resistivity intervals to account for this effect: (1) $[\boldsymbol{\rho} - \boldsymbol{\varepsilon}_{\mathbf{absolute}}; \boldsymbol{\rho} + \boldsymbol{\varepsilon}_{\mathbf{absolute}}]$ for cells with a resistivity close to approximately $\overline{\rho}$, (2) $[\boldsymbol{\rho} - \boldsymbol{\varepsilon}_{\mathbf{absolute}}; \boldsymbol{\rho}]$ for cells with a resistivity magnitude of less than approximately $\overline{\rho}$, and (3) $[\boldsymbol{\rho}; \boldsymbol{\rho} + \boldsymbol{\varepsilon}_{\mathbf{absolute}}]$ for cells with a resistivity amplitude of greater than approximately $\overline{\rho}$, where approximately $\overline{\rho}$ is a resistivity close to the median resistivity, i.e., ranging in $\overline{\rho}(1 \pm \gamma)$. Assuming an arbitrary value of $\gamma = 0.25$, our results suggest well-constrained resistivities of 20–50 and 90–110 ohm-m in LB and TL, respectively (Figures 7a, 7b, and 8). We obtain resistivities of 110–230 and 40–110 ohm-m in HB and BL, respectively (Figures 7d, 7e, and 8). Conversely, due to the presence of two anomalous bodies within ML, this layer remains poorly constrained with a resistivity of 10–160 ohm-m, even in the covered areas (Figures 7c and 8).

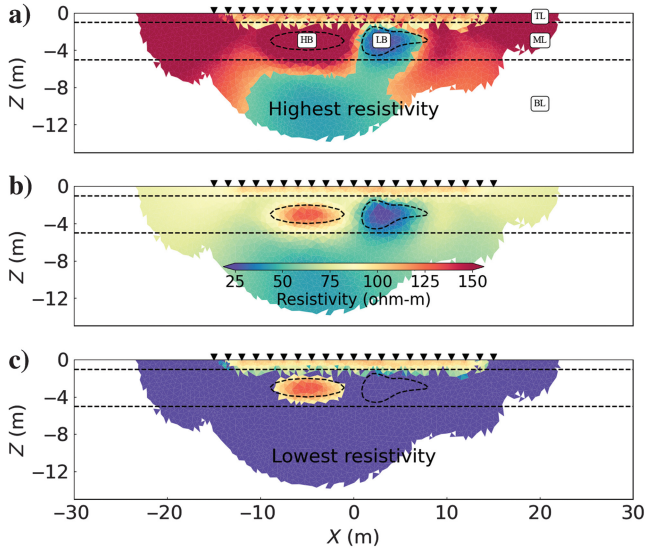

Figure 8. Absolute errors estimated from the PyMERRY algorithm. The dotted black lines indicate the location of the bodies in the true model. The black triangles show the electrode positions. The color scale represents the resistivity values in covered cells. Body names TL, ML, BL, HB, and LB are shown in Figure 4. (a) Highest resistivity values, (b) inversion-derived resistivity model, and (c) lowest resistivity values.

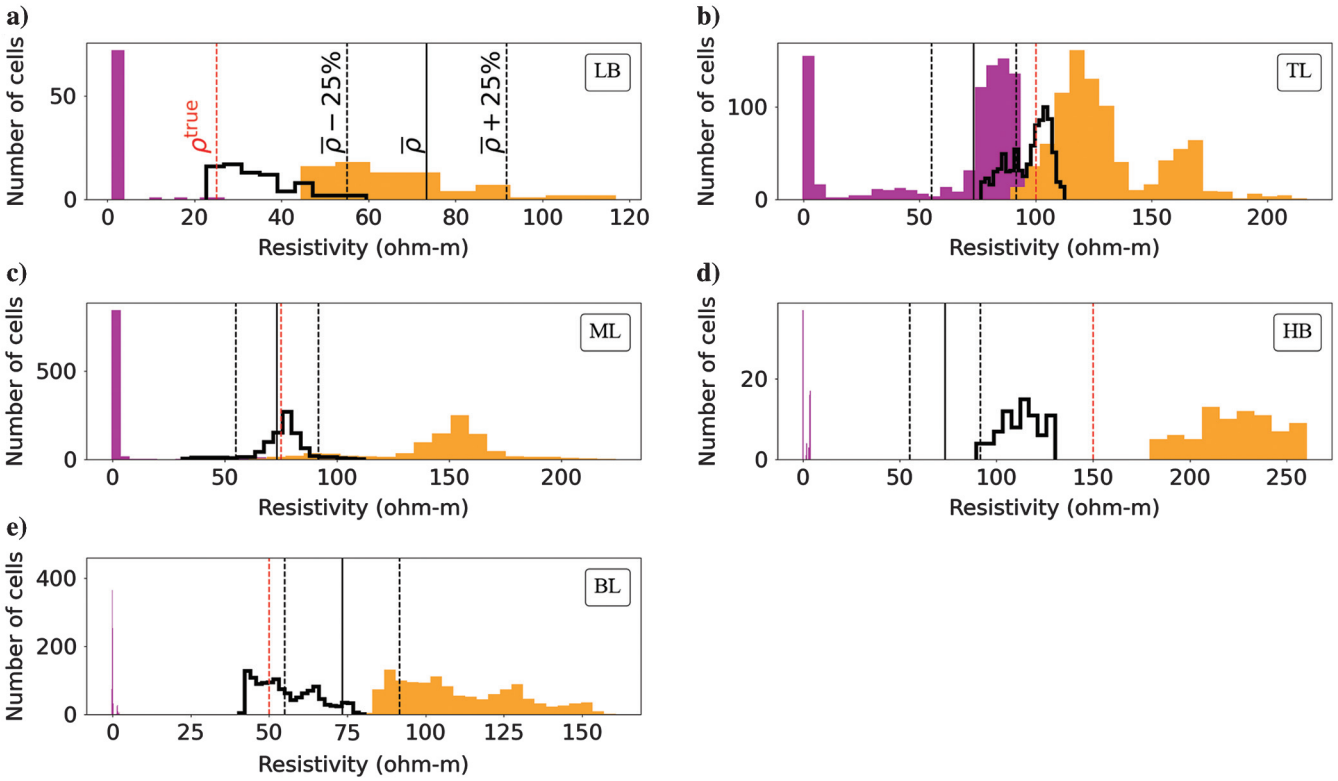

Figure 7. The PyMERRY absolute error and associated resistivity distribution obtained in each body of the true model. The purple, black, and orange histograms are related to $\boldsymbol{\rho} - \boldsymbol{\varepsilon}_{\mathbf{absolute}}$, $\boldsymbol{\rho}$, and $\boldsymbol{\rho} + \boldsymbol{\varepsilon}_{\mathbf{absolute}}$ distributions, respectively, with $\boldsymbol{\rho}$ the inversion-derived resistivity model and $\boldsymbol{\varepsilon}_{\mathbf{absolute}}$ the absolute error estimated with PyMERRY. Only the covered cells are shown. Body names TL, ML, BL, HB, and LB are shown in Figure 4. The dotted red line shows the true resistivity ρ^{true}. The black lines are associated with the mean of resistivity model $\boldsymbol{\rho}$. (a) Resistivity distribution obtained in LB, (b) the same as (a) for TL, (c) the same as (a) for ML, (d) the same as (a) for HB, and (e) the same as (a) for BL.

In this section, the presented results are for a dipole-dipole configuration. The use of other configurations such as Wenner or Wenner-Schlumberger confirms the robustness of the reliability criteria implemented in PyMERRY (see Appendix D). Using a mask based on coverage and considering the instrumental error allows us to quantify the resolution and the errors of an ERT image. In the following, we apply our approach to a real data set acquired along the southern edge of the Himalayas.

APPLICATION TO THE BHUTAN HIMALAYA

Site description and data

It is now well established that the intense seismic activity observed along the Himalayan arc is related to the India-Eurasia collision. The shortening rate between these two continental plates leads to a slow stress accumulation in the upper crust, which is transferred to the surface during the largest seismic events (Cattin and Avouac, 2000). The associated slip occurs along thrust faults reaching the surface at the topographic front. Better constraining the geometry of TFT is thus essential to improving the seismic hazard assessment in Nepal, Bhutan, and northern India, one of the most densely populated regions.

Our approach is applied in Sarpang, a small town in south-central Bhutan (Figure 9), where a host of information is available regarding seismic behavior, in particular Holocene deformation and active fault geometry. This area experienced at least two major earthquakes in the last millennium, one in 1714 and one during medieval times. Both events occurred along the TFT, producing a total cumulative vertical offset larger than 10 m (e.g., Hetenyi et al., 2016; Le Roux-Mallouf et al., 2016). Tectonic scarps and well-preserved abandoned terraces on both banks of the Sarpang River also attest to the accumulation of vertical deformation through time, suggesting a steep TFT near the surface (Berthet et al., 2014). This geometry is confirmed by structural observations (Long et al., 2011) and subsurface geophysical images obtained from electrical resistivity, seismic refraction, and microgravimetry surveys conducted in this area (Drukpa, 2017).

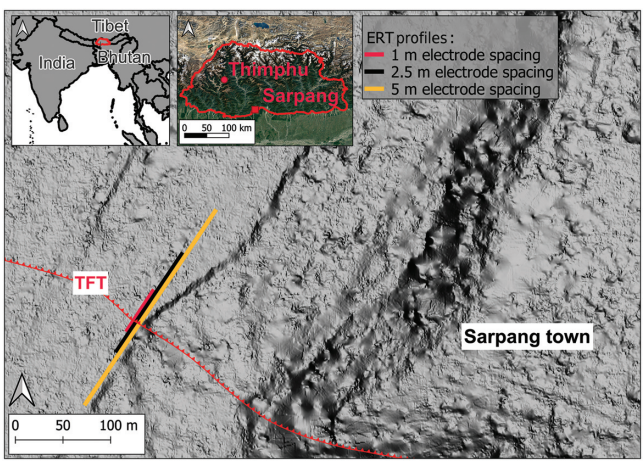

Figure 9. Shaded relief obtained from a 1 m resolution Pleiades digital elevation model. This map shows the site of the ERT experiment conducted on the southern edge of the Himalayas range. Insets give the location of the Kingdom of Bhutan (the red contour) and the study area of Sarpang in south-central Bhutan (the red square). The map shows the location of the three ERT profiles near Sarpang, with electrode spacing ranging from 1 to 5 m. The line of red triangles marks the trace of the TFT.

Taking advantage of the availability of electrical measurements, we revisit the ERT images proposed by Drukpa (2017) and Drukpa et al. (2018). After filtering to remove outliers or measurements with high errors, the data set consists of 3×558 apparent resistivity measurements acquired with a Syscal Pro Switch resistivity meter along three profiles of 48 electrodes spaced at 1, 2.5, and 5 m in a Wenner-Schlumberger configuration (Figure 9). The data sheet of the used resistivity meter indicates nominal instrumental accuracies of $\alpha = 0.002$ and $\beta = 0.002$ for current injection and potential measurement, respectively. Without additional information about the instrumental parameters during these field acquisitions, we use these values to fix the instrumental detectability threshold.

Inversion and PyMERRY results

We perform inversion using PyGIMLi for the three ERT profiles. We assume a homogeneous starting model based on median apparent resistivity data for each one and use a regularization parameter of $\lambda = 20$. This starting model and regularization choice refer to the default settings in the PyGIMLi inversion scheme. We perform the inversion on a mesh centered on the ERT profiles. We extend the mesh laterally and in-depth by half the length of the profile to avoid edge effects. Finally, a mesh refinement is applied near the electrodes as the PyGIMLi documentation website advises. For the three profiles, the algorithm returns the best resistivity model after five or six iterations with an associated root mean square of approximately 11%–17%. Chi-square values decreased by 99% (from 435 to 0.89), 99% (from 1017 to 4.48), and 99% (from 774 to 2.73) and converged to a plateau for inversion of 1, 2.5, and 5 m electrode spacing profile data sets, respectively. The three inverted ERT profiles give consistent results. Hence, we discuss the results obtained for the profile with an electrode spacing of 2.5 m (Figure 10). The results of the two other profiles are shown in Appendix E.

In agreement with the main results of Drukpa et al. (2018), the obtained ERT model suggests a steep TFT well imaged by a resistivity contrast ratio (approximately 1:100) between its two sides (Figure 10b). The south side shows relatively constant resistivity values with a very high-resistivity zone at a depth of 3–20 m. The north side shows a resistivity layering with a thin upper layer resistivity of approximately 400 ohm-m overlaying a layer with very low resistivity (lower than 100 ohm-m) that decreases laterally.

In this case study, one run with the PyMERRY code takes approximately 10 min on a 32-core CPU workstation. The mask obtained with PyMERRY highlights a significant difference in the coverage between the two sides of the TFT. Indeed, as shown for the synthetic tests, the higher the resistivity, the less the area is correctly covered. Due to the resistivity contrast, only the 10 upper meters on the southern side are covered, whereas the image remains robust up to 25 m on the north side. Unsurprisingly, the relative error increases with the distance to the electrodes (Figure 10d). It is small, <5% in the upper part of the covered area, and increases with depth to reach up to 100%. The main exception is located on the northern edge of the fault, where the lowest resistivity layers favor a high current density. This result illustrates the complementarity between the proposed calculation of the relative error and the standard sensitivity map (Figure 10d and 10e). Indeed, these two quantities show similarities, particularly by highlighting

areas of low resistivity associated with a high sensitivity and a low relative error. It also shows significant differences, especially near the surface where the sensitivities obtained are low, whereas the relative errors remain low. The sensitivity is dependent on the current density only. Relatively resistive areas, such as the surface layers of this model, are therefore associated with low current density. In contrast, the relative errors, which depend on current density and coverage, remain low for resistive areas close to the electrodes.

The two profiles associated with the lowest and the highest resistivities provide valuable information (Figure 10a–10c). We confirm the conclusions of Drukpa et al. (2018), retrieving the main features described previously for Figure 10b with high electrical resistivity contrasts across the fault zone with a nearly vertical contact down to approximately 25 m depth. The two profiles also allow for a more detailed interpretation, considering small-scale variations. The uncertainty analysis of the ERT model supports the reliability of the image obtained on the south side. It reveals a resistivity layering with a thin upper layer of high resistivity (approximately 1000 ohm-m) covering a layer with very high resistivity (>5000 ohm-m) that decreases beyond approximately a 20 m depth. The analysis also suggests a southward increase in the resistivity of the upper layer.

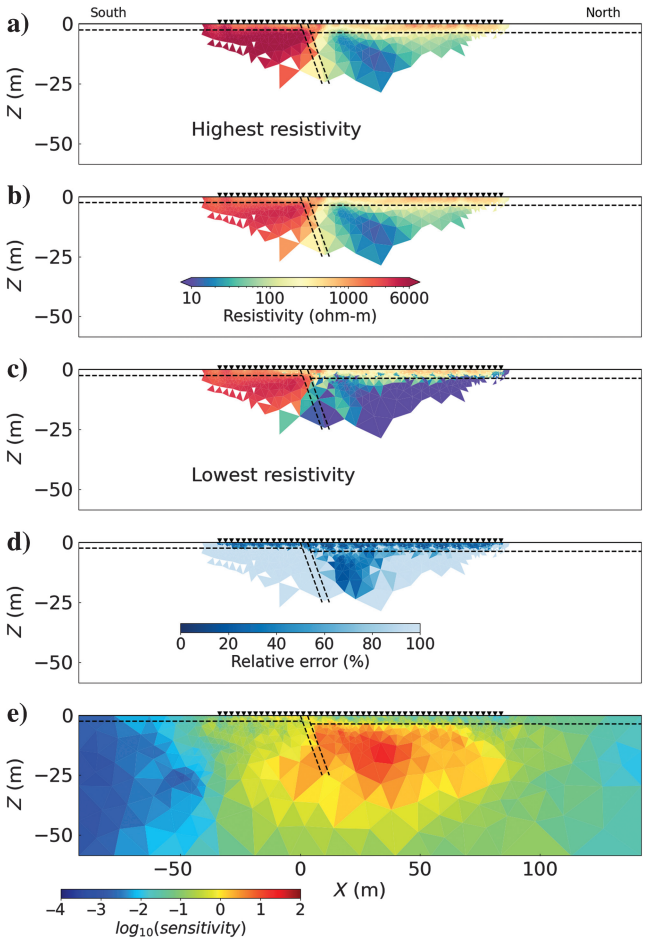

Figure 10. South–north resistivity section and associated reliability. The ERT image is obtained from the inversion of a Wenner-Schlumberger data set with 2.5 m electrode spacing collected in south-central Bhutan (see location Figure 9). The dotted black lines represent the best model proposed by Drukpa et al. (2018). The black triangles show the electrode positions. (a–c) ERT images and associated absolute errors. The color bar indicates the resistivity values. (d) Relative error map. (e) Sensitivity map used in the PyGIMLi inversions process. The color bar indicates the logarithm of sensitivity.

Conversely, part of the outcomes obtained on the northern side seems less reliable. Unlike the model derived from inversion (Figure 10b), the lowest resistivity model suggests that the lower layer on the north side could have a very low uniform resistivity of 10 ohm-m (Figure 10c). Therefore, any lateral and depth changes that are visualized by the inversion on the north side should be carefully interpreted.

The ERT models obtained using electrode spacings of 1 and 5 m provide additional support and details regarding these findings. They suggest a fault with a steep slope down to a depth of 50 m, with local and depth variations in resistivity on the south side. In addition, they confirm a 4 m thick homogeneous layer with a resistivity of approximately 800 ohm-m, overlaying a zone of very low resistivity on the north side (Appendix E).

CONCLUSION

This paper introduces a new tool for analyzing the reliability of ERT models. Thanks to the PyGIMLi library, we propose an approach based on the Fréchet derivative calculations, which considers the specificities of field experiments and instrumental constraints. This postprocessing tool provides two original outputs: a coverage mask and relative/absolute error maps associated with ERT models generated by software such as Res2Dinv, R2, or PyGIMLi. Synthetic data tests show the robustness of the implemented criteria. Using a mask based on coverage and considering the instrumental error allow us to quantify the resolution and the errors of an ERT image. Application to the Bhutan Himalaya underlines the benefits of our approach in reducing ambiguities in the ERT images. It also reveals the existence of small-scale lateral variations.

Our method offers complementary information compared with traditional sensitivity approaches, which only depend on current density. Our relative error approach seems better suited for interpreting areas with high-resistivity contrast. Furthermore, by providing a minimum and maximum resistivity value for each cell, our approach allows a more straightforward interpretation of the ERT results. The synthetic case and the field-based example presented in this study underline the relevance of PyMERRY for tabular or subvertical structures with low- or high-resistivity contrasts.

The definition of an a priori mesh used in the inversion remains a significant limitation of the ERT model's interpretation. Our approach considers, via the coverage, the mesh's geometry by including the size of each cell. Thus, a tiny resistive mesh size close to the electrodes can have the same relative error as a sizable conductive mesh far from the electrodes. Developing an adapted mesh, which would allow a homogeneous relative error, would facilitate the interpretation of ERT images.

Finally, future studies include applying this tool for 3D geometries with topography variations, time-lapse monitoring, and extending the approach to joint inversion procedures associated with other near-surface geophysical data.

ACKNOWLEDGMENTS

We would like to thank A. Binley for his particularly constructive review of this paper and the two other anonymous reviewers. We also

thank the members of the editorial board of GEOPHYSICS: A. Malcolm, editor-in-chief, M. Ravasi, associate editor, and E. Saenger, assistant editor, for their constructive feedback on the manuscript and associated code.

M. Gautier's Ph.D. is supported by a fellowship from the French Ministry for Higher Education and Research. This study was supported by the Agence Nationale de la Recherche (France): project TopoExtreme (PI: R.C. — grant ANR-18-CE01-0017). The Bhutan surveys benefited from the support of the French RESIF Research Infrastructure (http://www.resif.fr). These field campaigns would not have been possible without the unfailing support of the staff and drivers of the Department of Geology and Mines, Bhutan.

DATA AND MATERIALS AVAILABILITY

Data associated with this research are available and can be obtained by contacting the corresponding author.

APPENDIX A

TABLE OF SYMBOLS

The complete table of symbols used in this study is shown in Table A-1.

Table A-1. Used symbols.

Symbol	Unit	Description
n	∅	Number of data/quadrupoles
j, i	∅	jth quadrupole and ith cell
A, B, M, N	∅	A-B: injection electrodes and M-N: potential electrodes
$\boldsymbol{\rho_a}$	ohm-m	Apparent resistivity measured in the field
$\boldsymbol{\rho_a^{th}}$, $\rho_a^{j,\mathrm{th}}$	ohm-m	Synthetic apparent resistivity computed on the model returned by the inversion process
$\boldsymbol{\rho_a^{var}}$	ohm-m	Apparent resistivity measured after a modification in a model
$\boldsymbol{\rho}, \rho_i$	ohm-m	Resistivity model and resistivity value in the cell
ρ^{true}	ohm-m	The true value of resistivity in a synthetic model
$\overline{\rho}$	ohm-m	The mean value of the resistivity model in covered cells
$\delta\boldsymbol{\rho}, \delta\rho_i, \delta\rho_i^{j,+}, \delta\rho_i^{j,-}, \delta\rho_i^j$	ohm-m	Resistivity model variation
$\mathbf{J}, \mathbf{J}_\mathrm{A}, \mathbf{J}_\mathrm{M}, \mathbf{J}_\mathrm{A}^j, \mathbf{J}_\mathrm{B}^j, \mathbf{J}_\mathrm{M}^j, \mathbf{J}_\mathrm{N}^j$	A.m^{-2}	Current density associated with electrodes and quadrupoles
$\mathbf{F}^j, F_i^j, F_{\mathrm{DOI}}^j$	A.m^{-4}	Fréchet derivative associated with quadrupole, cell, and DOI
DOI	m	Depth of investigation
$\boldsymbol{\varepsilon}, \boldsymbol{\varepsilon_{\mathrm{relative}}}, \boldsymbol{\varepsilon_{\mathrm{absolute}}}$	% or ohm-m	Error on the resistivity model
$\mathbf{m}^j, m_i^j$	∅	Binary mask for a quadrupole
C_i	∅	Coverage
V, dV	m^3	Volume and elementary volume
$R, \partial R$	ohm	Resistivity and resistivity variation
$\mathbf{U}, U, \delta\mathbf{U}, \partial U$	V	Potential and potential variation
$I, \partial I$	A	Current intensity and intensity variation
k^j	m	Geometric factor of a quadrupole
t^j	ohm-m	Instrumental threshold for a quadrupole
$\Delta\rho_a^{j,\mathrm{instrument}}$	ohm-m	Variation between the theoretical apparent resistivity on the inversion image and a model with a resistivity variation in a cell
$\rho_a^{j,\mathrm{var}}$	ohm-m	Theoretical apparent resistivity on a model with a resistivity variation in a cell
γ	%	Deviation from the resistivity mean value
α, β	%	Resistivity meter's nominal accuracies on injected current and received potential
λ	∅	Regularization parameter in the inversion scheme
TL, ML, BL, HB, LB	∅	Bodies names: TL, top layer; ML, middle layer; BL, bottom layer; HB, high-resistivity body; and LB, low-resistivity body
∇	∅	Nabla operator
L	m	Length of the quadrupole
$f_i(\mathrm{mod})$	ohm-m	Forward response of a model called mod
Φ_d	∅	Objective function data misfit
d_i	ohm-m	Data measured by the jth quadrupole
σ_i	ohm-m	Standard deviation on the data measured by the jth quadrupole
χ^2	∅	Chi-squared value

APPENDIX B

INSTRUMENTAL THRESHOLD CALCULATION

Ohm's law gives a link between the resistance R, current intensity I, and potential U:

$$R = \frac{U}{I}. \tag{B-1}$$

Partial derivatives of this equation are $(\partial R(U)/\partial U) = (1/I)$ and $(\partial R(I)/\partial I) = (-U/I^2)$. A variation of resistivity ∂R is caused by a variation of potential ∂U and/or a variation of intensity ∂I. Let us consider the sum of their absolute values in

$$\partial R = \frac{1}{I}\partial U + \frac{U}{I^2}\partial I. \tag{B-2}$$

We set $\partial U = \alpha U$ and $\partial I = \beta I$ with α and β nominal accuracies available on the resistivity meter technical manual. Therefore, equation B-2 becomes

$$\partial R = \frac{1}{I}\alpha U + \frac{U}{I^2}\beta I = (\alpha + \beta)\frac{U}{I} = (\alpha + \beta)R. \tag{B-3}$$

By comparing equations B-2 and B-3, the instrumental threshold t^j of the quadrupole j corresponds to a resistance variation ∂R and the resistance R to an apparent resistivity by taking into account of the geometric factor k^j. Therefore, the threshold t^j is given by

$$t^j = (\alpha + \beta)|k^j|\rho_a^j. \tag{B-4}$$

APPENDIX C

DEFINITION OF THE CHI-SQUARED VALUE USED IN PYGIMLI

During the inversion process, the Gauss-Newton algorithm tries to minimize an objective function:

$$\Phi_d = \sum_{j=1}^{n}\left(\frac{d_j - f_j(\text{mod})}{\sigma_j}\right)^2, \tag{C-1}$$

where d_j is the observation j associated with the error σ_j and n is the number of observations. This function is the $L2$ norm of the misfit between field data and the forward response $f_j(m)$ for a given model mod. Then, the chi-squared value is defined as

$$\chi^2 = \frac{\Phi_d}{n}. \tag{C-2}$$

APPENDIX D

SYNTHETIC CASES FOR WENNER AND WENNER-SCHLUMBERGER ARRAYS

Figures 4–8 refer to the synthetic case with dipole-dipole configurations. The same figures are presented for Wenner (Figures D-1–D-5) and Wenner-Schlumberger configurations (Figures D-6–D-10).

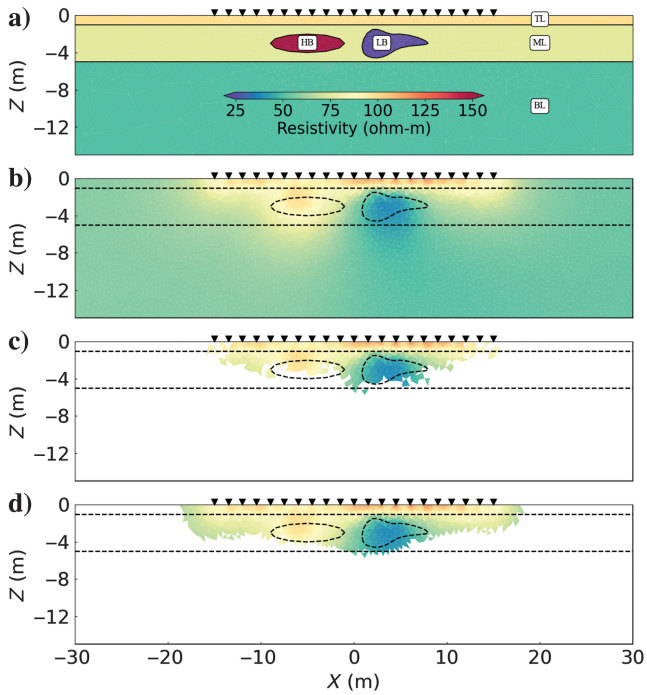

Figure D-1. The same as Figure 4 for the Wenner configuration.

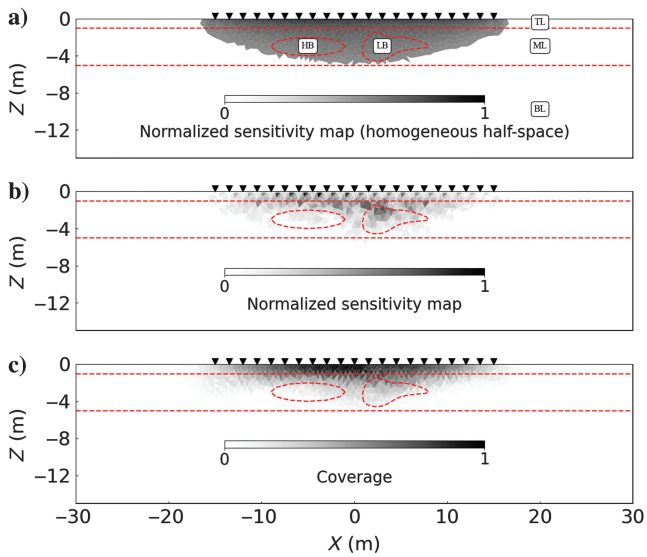

Figure D-2. The same as Figure 5 for the Wenner configuration.

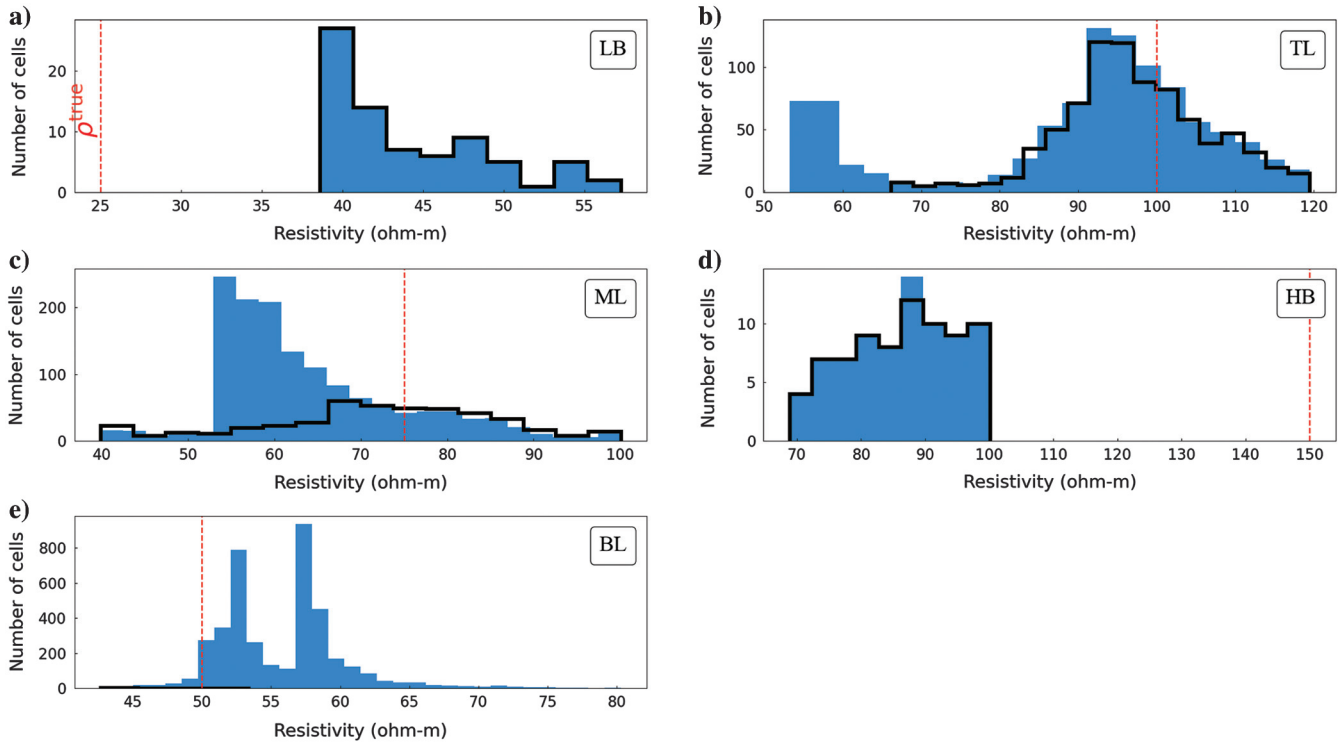

Figure D-3. The same as Figure 6 for the Wenner configuration.

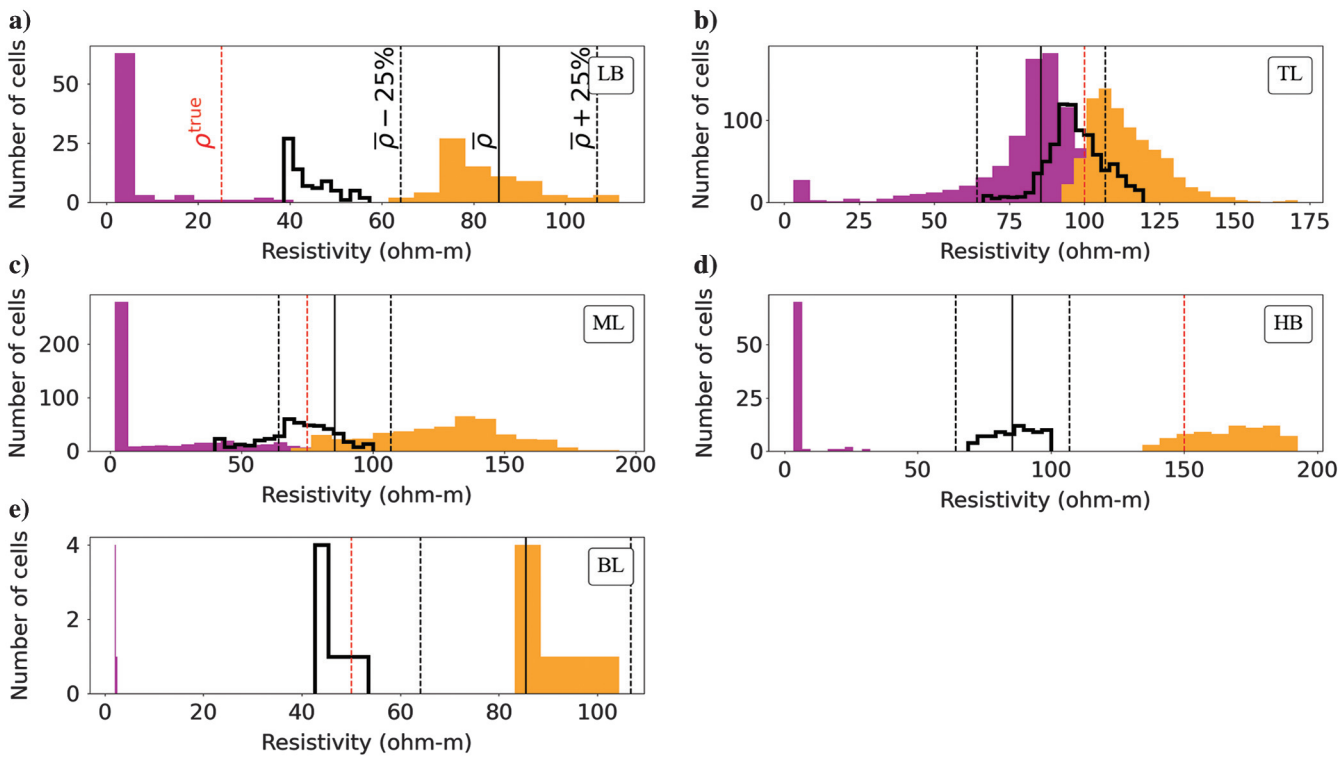

Figure D-4. The same as Figure 7 for the Wenner configuration.

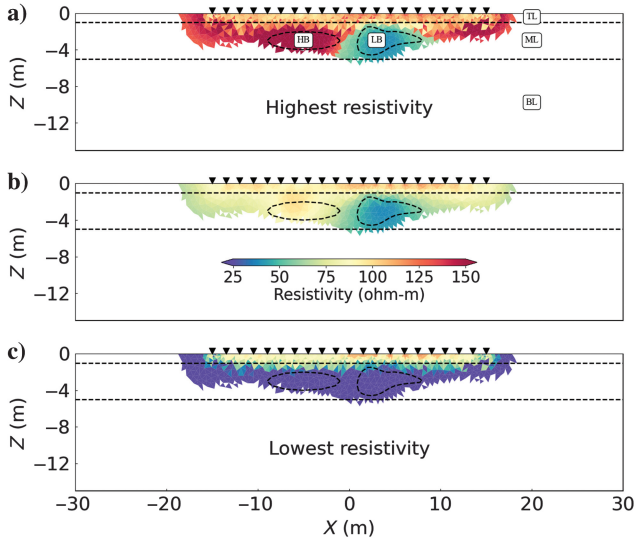

Figure D-5. The same as Figure 8 for the Wenner configuration.

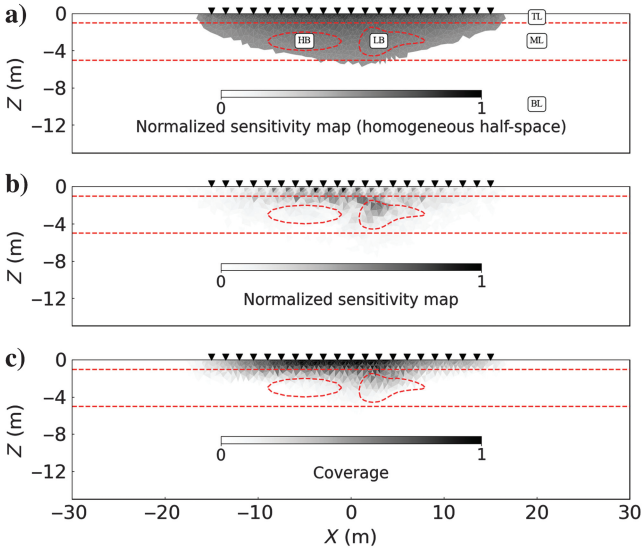

Figure D-7. The same as Figure 5 for the Wenner-Schlumberger configuration.

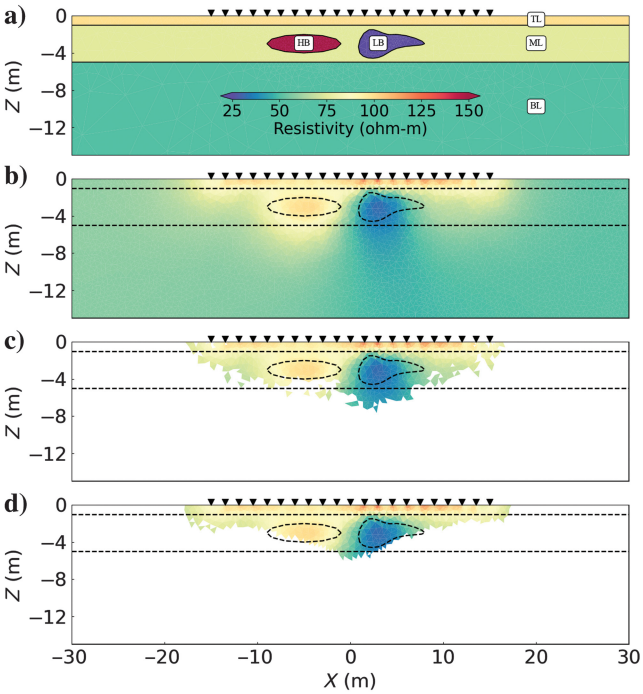

Figure D-6. The same as Figure 4 for the Wenner-Schlumberger configuration.

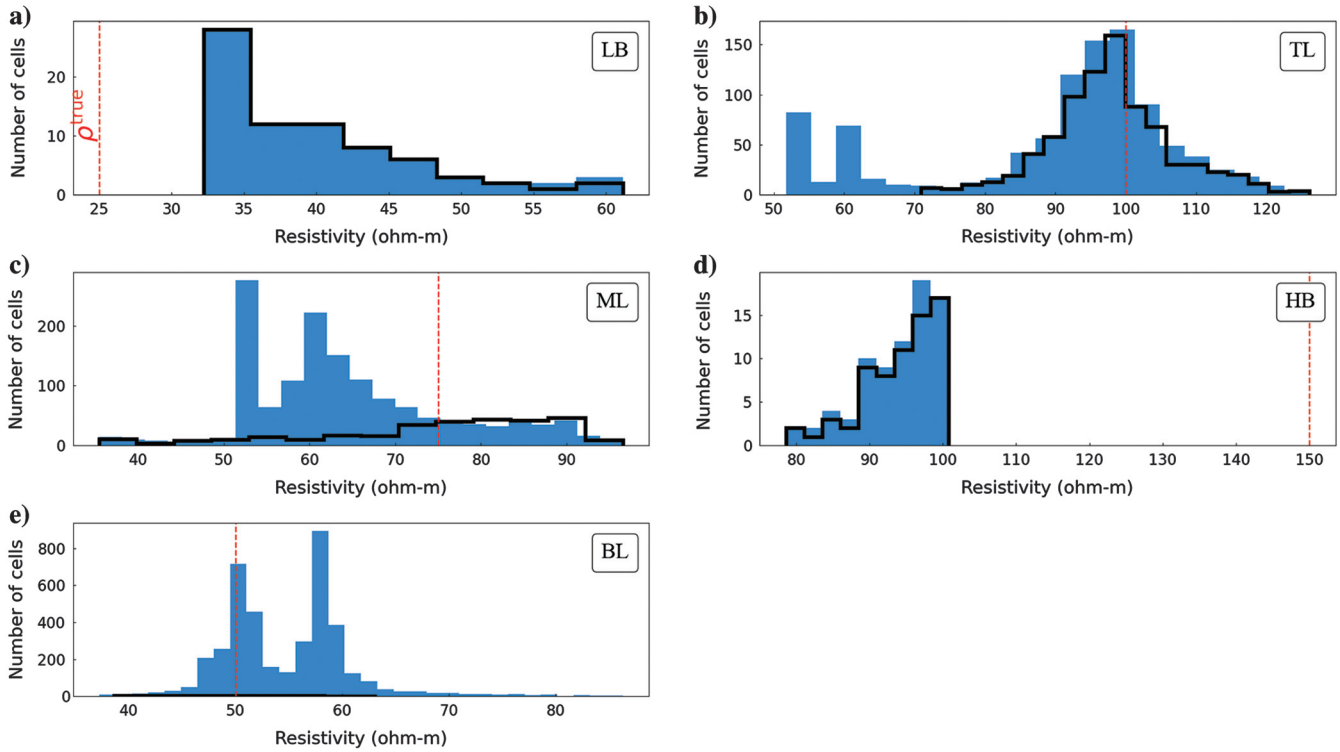

Figure D-8. The same as Figure 6 for the Wenner-Schlumberger configuration.

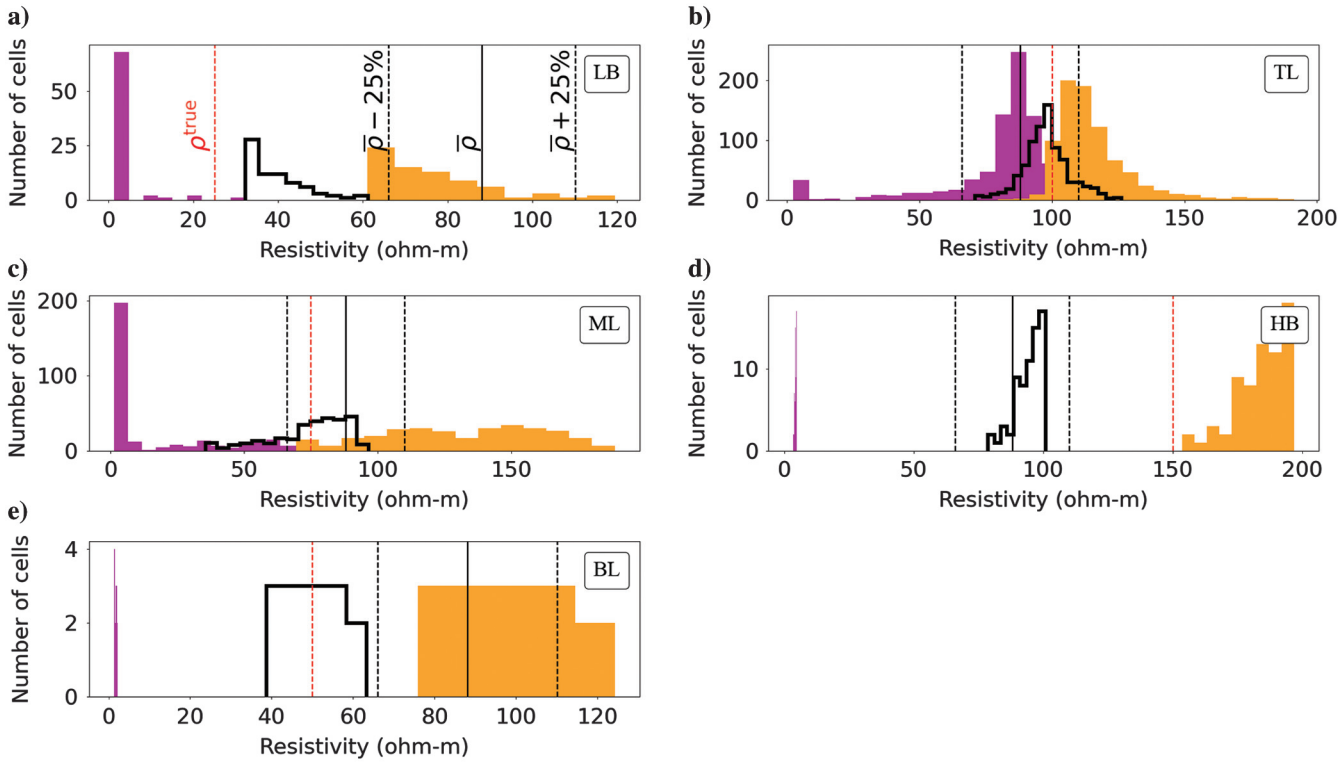

Figure D-9. The same as Figure 7 for the Wenner-Schlumberger configuration.

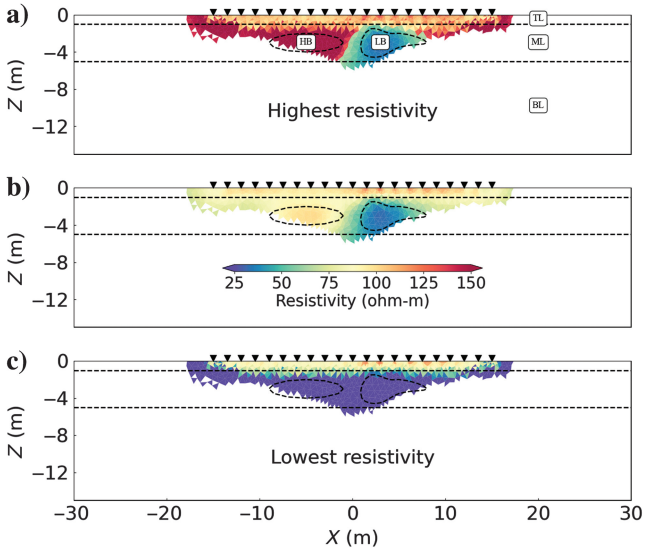

Figure D-10. The same as Figure 8 for the Wenner-Schlumberger configuration.

APPENDIX E

INVERSION AND PYMERRY RESULTS FROM 1 AND 5 M ELECTRODE SPACING DATA SETS

During the geophysical campaign in Bhutan, three ERT data sets were collected with a 48 electrodes survey, with 1, 2.5, and 5 m electrode spacing. These profiles are all located on the map in Figure 9. Here, we present the inversion and postprocessing analyses for 1 and 5 m electrode spacing profiles (Figures E-1 and E-2). They suggest the same interpretation as results related to the 2.5 m electrode spacing profile, presented in the "Application to the Bhutan Himalaya" section.

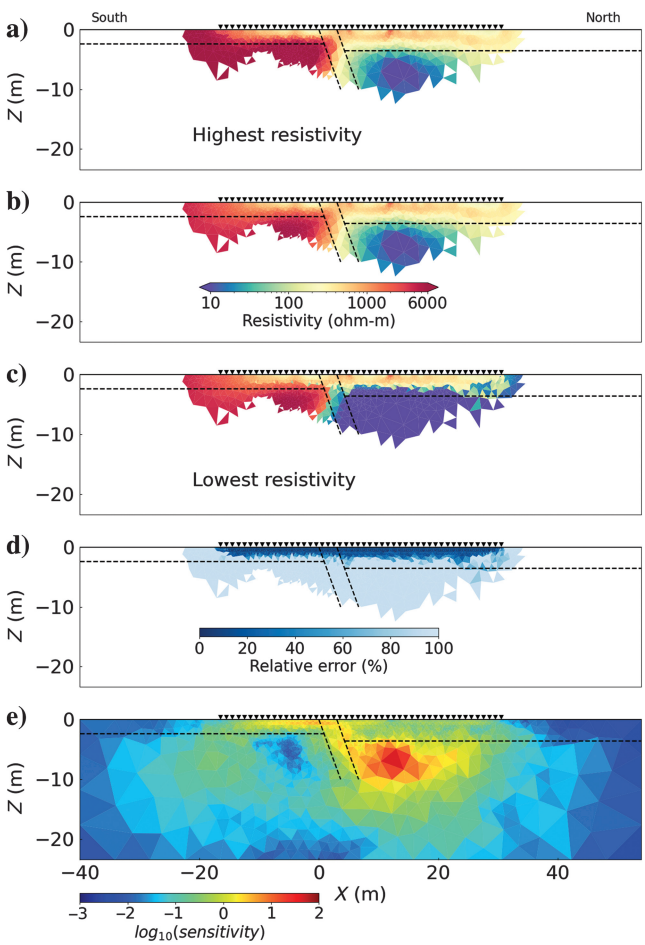

Figure E-1. The same as Figure 10, using an electrode spacing of 1 m.

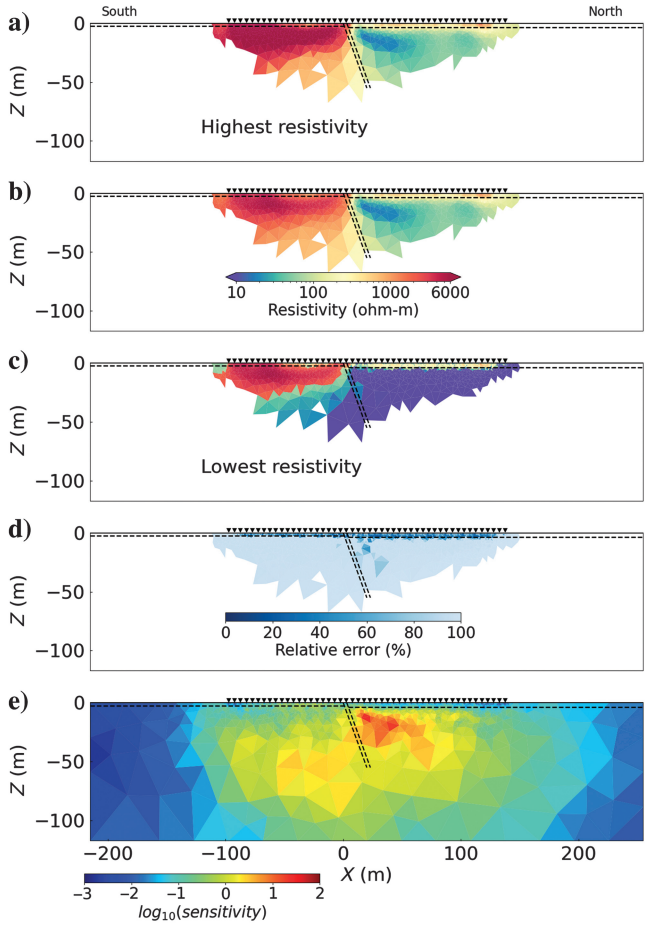

Figure E-2. The same as Figure 10, using an electrode spacing of 5 m.

REFERENCES

Barker, R. D., 1989, Depth of investigation of collinear symmetrical four-electrode arrays: Geophysics, **54**, 1031–1037, doi: 10.1190/1.1442728.

Bergmann, P., C. Schmidt-Hattenberger, D. Kiessling, C. Rücker, T. Labitzke, J. Henninges, G. Baumann, and H. T. Schütt, 2012, Surface-downhole electrical resistivity tomography applied to monitoring of CO_2 storage at Ketzin, Germany: Geophysics, **77**, no. 6, B253–B267, doi: 10.1190/geo2011-0515.1.

Berthet, T., J.-F. Ritz, M. Ferry, P. Pelgay, R. Cattin, D. Drukpa, R. Braucher, and G. Hetenyi, 2014, Active tectonics of the eastern Himalaya: New constraints from the first tectonic geomorphology study in southern Bhutan: Geology, **42**, 427–430, doi: 10.1130/G35162.1.

Binley, A., G. Cassiani, R. Middleton, and P. Winship, 2001, Vadose zone flow model parametrisation using cross-borehole radar and resistivity imaging: Journal of Hydrology, **267**, 147–159, doi: 10.1016/S0022-1694(02)00146-4.

Binley, A., and A. Kemna, 2005, DC resistivity and induced polarization methods, *in* Y. Rubin and S. S. Hubbard, eds., Hydrogeophysics: Springer, Water Science and Technology Library 50.

Binley, A., and L. Slater, 2020, Resistivity and induced polarization. Theory and applications to the near-surface earth: Cambridge University Press, 388.

Cattin, R., and J. P. Avouac, 2000, Modeling mountain building and the seismic cycle in the Himalaya of Nepal: Journal of Geophysical Research: Solid Earth, **105**, 13389–13407, doi: 10.1029/2000JB900032.

Daily, W., and A. L. Ramirez, 2000, Electrical imaging of engineered hydraulic barriers: Geophysics, **65**, 83–94, doi: 10.1190/1.1444728.

Danielsen, B. E., and T. Dahlin, 2010, Numerical modelling of resolution and sensitivity of ERT in horizontal boreholes: Journal of Applied Geophysics, **70**, 245–254, doi: 10.1016/j.jappgeo.2010.01.005.

Demanet, D., E. Pirard, F. Renardy, and D. Jongmans, 2001, Application and processing of geophysical images for mapping faults: Computer & Geosciences, **27**, 1031–1037, doi: 10.1016/S0098-3004(00)00156-4.

Denchik, N., P. A. Pezard, D. Neyens, J. Lofi, F. Gal, J.-F. Girard, and A. Levannier, 2014, Near-surface CO_2 leak detection monitoring from downhole electrical resistivity at the CO_2 field laboratory, Svelvik Ridge (Norway): International Journal of Greenhouse Gas Control, **28**, 275–282, doi: 10.1016/j.ijggc.2014.06.033.

Dimech, A., L. Cheng, M. Chouteau, J. Chambers, S. Uhlemann, P. Wilkinson, P. Meldrum, B. Mary, G. Fabien-Ouellet, and A. Isabelle, 2022, A review on applications of time-lapse electrical resistivity tomography over the last 30 years: Perspectives for mining waste monitoring: Surveys in Geophysics, **43**, 1699–1759, doi: 10.1007/s10712-022-09731-2.

Drukpa, D., 2017, Imaging the main frontal thrust in southern Bhutan using high-resolution near-surface geophysical techniques: Implications for tectonic geomorphology and seismic hazard assessment: Ph.D. thesis, University of Montpellier.

Drukpa, D., S. Gautier, R. Cattin, K. Namgay, and N. Le Moigne, 2018, Impact of near-surface fault geometry on secular slip rate assessment derived from uplifted river terraces: Implications for convergence accommodation across the frontal thrust in southern Central Bhutan: Geophysical Journal International, **212**, 1315–1330, doi: 10.1093/gji/ggx478.

Fortier, R., and M. Bolduc, 2008, Thaw settlement of degrading permafrost: A geohazard affecting the performance of man-made infrastructures at Umiujaq in Nunavik (Québec): 4th Canadian Conference on Geohazards: From Causes to Management.

Friedel, S., A. Thielen, and S. M. Springman, 2006, Investigation of a slope endangered by rainfall-induced landslides using 3D resistivity tomography and geotechnical testing: Journal of Applied Geophysics, **60**, 100–114, doi: 10.1016/j.jappgeo.2006.01.001.

Furman, A., T. P. A. Ferré, and A. W. Warrick, 2003, A sensitivity analysis of electrical resistivity tomography array types using analytical element modelling: Vadose Zone Journal, **2**, 416–423, doi: 10.2136/vzj2003.4160.

Gance, J., J.-P. Malet, R. Supper, P. Sailhac, D. Ottowitz, and B. Jochum, 2016, Permanent electrical resistivity measurements for monitoring water circulation in clayey landslides: Journal of Applied Geophysics, **126**, 98–115, doi: 10.1016/j.jappgeo.2016.01.011.

Ghanati, R., and M. Fallahsafari, 2022, Fréchet derivatives calculation for electrical resistivity imaging using forward matrix method: Iranian Journal of Geophysics, **15**, 153–163,doi: 10.30499/IJG.2021.283620.1325.

Günther, T., C. Rücker, and K. Spitzer 2006, Three-dimensional modelling and inversion of DC resistivity data incorporating topography: Geophysical Journal International, **166**, 506–517, doi: 10.1111/j.1365-246X.2006.03011.x.

Hetenyi, G., R. Le Roux-Mallouf, T. Berthet, R. Cattin, C. Cauzzi, K. Phuntsho, and R. Grolimund, 2016, Joint approach combining damage and paleoseismology observations constrains the 1714AD Bhutan earthquake at magnitude 8 ± 0.5: Geophysical Research Letters, **43**, 10695–10702, doi: 10.1002/2016GL071033.

Jomard, H., T. Lebourg, Y. Guglielmi, and E. Tric, 2010, Electrical imaging of sliding geometry and fluids associated with a deep seated landslide (La Clapière, France): Earth Surface Processes and Landforms, **35**, 588–599, doi: 10.1002/esp.1941.

Kuras, O., P. B. Wilkinson, P. I. Meldrum, L. S. Oxby, S. Uhlemann, J. E. Chambers, A. Binley, J. Graham, N. T. Smith, and N. Atherton, 2016, Geoelectrical monitoring of simulated subsurface leakage to support high-hazard nuclear decommissioning at the Sellafield site, UK: Science of the Total Environment, **566–567**, 350–359, doi: 10.1016/j.scitotenv.2016.04.212.

LaBrecque, D. J., W. Daily, and P. Adkins, 2007, Systematic errors in resistivity measurement systems: Proceedings of the Symposium on the Application of Geophysics to Engineering and Environmental Problems, 1153–1160.

LaBrecque, D. J., G. Morelli, W. Daily, A. Ramirez, and P. Lundegard, 1999, Occam's inversion of 3-D electrical resistivity tomography, *in* M. Oristaglio and B. Spies, eds., Three-dimensional electromagnetic: SEG, Geophysical Developments Series, 575–590.

Lapenna, V., and A. Perrone, 2022, Time-lapse electrical resistivity tomography (TL-ERT) for landslide monitoring: Recent advances and future directions: Applied Sciences, **12**, 1425, doi: 10.3390/app12031425.

Le Roux-Mallouf, R., M. Ferry, J. F. Ritz, T. Berthet, R. Cattin, and D. Drukpa, 2016, First paleoseismic evidence for great surface-rupturing earthquakes in the Bhutan Himalayas: Journal of Geophysical Research, **121**, 7271–7283, doi: 10.1002/2015JB012733.

Lévy, L., R. Thalund-Hansen, T. Bording, G. Fiandaca, A. V. Christiansen, K. Rügge, N. Tuxen, M. Hag, and P. L. Bjerg, 2022, Quantifying reagent spreading by cross-borehole electrical tomography to assess performance of groundwater remediation: Water Resources Research, **58**, e2022WR032218, doi: 10.1029/2022WR032218.

Loke, M. H., and R. D. Barker, 1995, Least-squares deconvolution of apparent resistivity pseudosections: Geophysics, **60**, 1682–1690, doi: 10.1190/1.1443900.

Loke, M. H., and R. D. Barker, 1996, Rapid least-squares inversion of apparent resistivity pseudosections using a quasi-Newton method: Geophysical Prospecting, **44**, 131–152, doi: 10.1111/j.1365-2478.1996.tb00142.x.

Long, S., N. McQuarrie, T. Tobgay, D. Grujic, and L. Hollister, 2011, Geologic map of Bhutan: Journal of Maps, **7**, 184–192, doi: 10.4113/jom.2011.1159.

McGillivray, P. R., and D. W. Oldenburg, 1990, Methods for calculating Fréchet derivatives and sensitivities for the non-linear inverse problem: A comparative study: Geophysical Prospecting, **38**, 499–524, doi: 10.1111/j.1365-2478.1990.tb01859.x.

McLachlan, P. J., J. E. Chambers, S. S. Uhlemann, and A. Binley, 2017, Geophysical characterisation of the groundwater–surface water interface: Advances in Water Resources, **109**, 302–319, doi: 10.1016/j.advwatres.2017.09.016.

Nguyen, F., S. Garambois, D. Jongmans, E. Pirard, and M. H. Loke, 2005, Image processing of 2D resistivity data for imaging faults: Journal of Applied Geophysics, **57**, 260–277, doi: 10.1016/j.jappgeo.2005.02.001.

Nguyen, F., A. Kemna, A. Antonsson, P. Engesgaard, O. Kuras, R. Ogilvy, J. Gisbert, S. Jorreto, and A. Pulido-Bosch, 2009, Characterization of seawater intrusion using 2D electrical imaging: Near Surface Geophysics, **7**, 377–390, doi: 10.3997/1873-0604.2009025.

Oldenborger, G. A., P. S. Routh, and M. D. Knoll, 2005, Sensitivity of electrical resistivity tomography data to electrode position errors: Geophysical Journal International, **163**, 1–9, doi: 10.1111/j.1365-246X.2005.02714.x.

Oldenburg, D. W., and Y. Li, 1999, Estimating depth of investigation in DC resistivity and IP surveys: Geophysics, **64**, 403–416, doi: 10.1190/1.1444545.

Palacios, A., J. J. Ledo, N. Linde, L. Luquot, F. Bellmunt, A. Folch, A. Marcuello, P. Queralt, P. A. Pezard, L. Martínez, L. Del Val, D. Bosch, and J. Carrera, 2020, Time-lapse cross-hole electrical resistivity tomography (CHERT) for monitoring seawater intrusion dynamics in a Mediterranean aquifer: Hydrology and Earth System Sciences, **24**, 2121–2139, doi: 10.5194/hess-24-2121-2020.

Park, S. K., and G. P. Van, 1991, Inversion of pole-pole data for 3-D resistivity structure beneath arrays of electrodes: Geophysics, **56**, 951–960, doi: 10.1190/1.1443128.

Pazzi, V., S. Morelli, and R. Fanti, 2019, A review of the advantages and limitations of geophysical investigations in landslide studies: International Journal of Geophysics, **2019**, 1, doi: 10.1155/2019/2983087.

Perrone, A., V. Lapenna, and S. Piscitelli, 2014, Electrical resistivity tomography technique for landslide investigation: A review: Earth-Science Reviews, **135**, 65–82, doi: 10.1016/j.earscirev.2014.04.002.

Ramirez, A., J. Nitao, W. Hanley, R. Aines, R. Glaser, S. Sengupta, K. Dyer, T. Hickling, and W. Daily, 2004, Stochastic inversion of electrical resistivity changes using a Markov chain Monte Carlo approach: Journal of Geophysical Research, **110**, 1–18, doi: 10.1029/2004JB003449.

Romero-Ruiz, A., N. Linde, T. Keller, and D. Or, 2018, A review of geophysical methods for soil structure characterization: Reviews of Geophysics, **56**, 672–697, doi: 10.1029/2018RG000611.
Ronczka, M., K. Hellman, T. Günther, R. Wisén, and T. Dahlin, 2017, Electric resistivity and seismic refraction tomography: A challenging joint underwater survey at Äspö Hard Rock Laboratory: Solid Earth, **8**, 671–682, doi: 10.5194/se-8-671-2017.
Roy, A., and A. Apparao, 1971, Depth of investigation in direct current methods: Geophysics, **36**, 943–959, doi: 10.1190/1.1440226.
Rücker, C., T. Günther, F. Wagner, F. Dinsel, M. Weigand, and A. Balza, 2022, https://www.pygimli.org/_examples_auto/, accessed 10 June 2022.
Rücker, C., T. Günther, and F. M. Wagner, 2017, PyGIMLi: An open-source library for modelling and inversion in geophysics: Computers & Geosciences, **109**, 106–123, doi: 10.1016/j.cageo.2017.07.011.
Singha, K., F. D. Day-Lewis, T. Johnson, and L. D. Slater, 2015, Advances in interpretation of subsurface processes with time-lapse electrical imaging: Hydrological Processes, **29**, 1549–1576, doi: 10.1002/hyp.10280.
Suski, B., G. Y. Brocard, C. Authemayou, B. Consenza Muralles, C. Teyssier, and K. Holliger, 2010, Localization and characterization of an active fault in an urbanized area in central Guatemala by means of geoelectrical imaging: Tectonophysics, **480**, 88–98, doi: 10.1016/j.tecto.2009.09.028.
Telford, W., L. P. Geldart, and R. Sheriff, 1990, Applied geophysics, 2nd ed.: Cambridge University Press.
Tso, C.-H., O. Kuras, P. B. Wilkinson, S. Uhlemann, J. E. Chamber, P. I. Meldrum, J. Graham, E. F. Sherlock, and A. Binley, 2017, Improved characterisation and modelling of measurement errors in electrical resistivity tomography (ERT) surveys: Journal of Applied Geophysics, **146**, 103–119, doi: 10.1016/j.jappgeo.2017.09.009.
Villani, F., V. Tulliani, V. Sapia, E. Fierro, R. Civico, and D. Pantosti, 2015, Shallow subsurface imaging of the Piano Di Pezza active normal fault (central Italy) by high-resolution refraction and electrical resistivity tomography coupled with time-domain electromagnetic data: Geophysical Journal International, **203**, 1482–1494, doi: 10.1093/gji/ggv399.
Watlet, A., O. Kaufmann, A. Triantafyllou, A. Poulain, J. E. Chambers, P. I. Meldrum, P. B. Wilkinson, V. Hallet, Y. Quinifl, M. Van Ruymbeke, and M. Van Camp, 2018, Imaging groundwater infiltration dynamics in the karst vadose zone with long-term ERT monitoring: Hydrology and Earth System Sciences, **22**, 1563–1592, doi: 10.5194/hess-22-1563-2018.
Whiteley, J. S., J. E. Chambers, S. Uhlemann, P. B. Wilkinson, and J. M. Kendall, 2019, Geophysical monitoring of moisture-induced landslides: A review: Reviews of Geophysics, **57**, 106–145, doi: 10.1029/2018RG000603.
Wilkinson, P. B., P. I. Meldrum, O. Kuras, J. E. Chambers, S. J. Holyoake, and R. D. Ogilvy, 2010, High-resolution electrical resistivity tomography monitoring of a tracer test in a confined aquifer: Journal of Applied Geophysics, **70**, 268–276, doi: 10.1016/j.jappgeo.2009.08.001.
Zhou, B., and T. Dahlin, 2003, Properties and effects of measurement errors on 2D resistivity imaging surveying: Near Surface Geophysics, **1**, 105, doi: 10.3997/1873-0604.2003001.
Zhou, Q., X. Yang, R. Zhang, S. A. Hosseini, J. B. Ajo-Franklin, B. M. Freifeld, T. M. Daley, and S. D. Hovorka, 2020, Dynamic processes of CO_2 storage in the field: Multiscale and multipath channeling of CO_2 flow in the Hierarchical Fluvial Reservoir at Cranfield, Mississippi: Water Resources Research, **56**, e2019EF001360, doi: 10.1029/2019WR025688.

Biographies and photographs of the authors are not available.